

Passive All-Optical Nonlinear Neuron Activation via PPLN Nanophotonic Waveguides

Wujie Fu^{1,2,†}, Xiaodong Shi^{3,†}, Lei Shi¹, Sakthi Sanjeev Mohanraj³, Yuan Gao¹, Luo Qi¹, Pragati Aashna¹, Zexian Wang¹, Guanyu Chen^{4,5}, Di Zhu^{3,6,*}, and Aaron Danner^{1,2,*}

¹Department of Electrical and Computer Engineering, National University of Singapore, 117583, Singapore

²Graduate School for Integrative Sciences and Engineering, National University of Singapore, 119077, Singapore

³Quantum Innovation Centre (Q.InC), Institute of Materials Research and Engineering (IMRE), Agency for Science, Technology and Research (A*STAR), 138634, Singapore

⁴Key Laboratory of Optoelectronic Technology & Systems Ministry of Education, Chongqing University, Chongqing 400044, China

⁵College of Optoelectronic Engineering, Chongqing University, Chongqing 400044, China

⁶Department of Materials Science and Engineering, National University of Singapore, 117575, Singapore

[†]These authors contributed equally.

*Corresponding authors: adanner@nus.edu.sg; dizhu@nus.edu.sg

ABSTRACT

Artificial intelligence (AI) is transforming modern life, yet the growing scale of AI applications places mounting demands on computational resources, raising sustainability concerns. Photonic integrated circuits (PICs) offer a promising alternative, enabling massive parallelism, low latency, and reduced electrical overhead, particularly excelling in high-throughput linear operations. However, passive and fully optical nonlinear activation functions with equally superb performance remain rare, posing a critical bottleneck in realizing all-optical neural networks on PICs. Here, we demonstrate a compact and readily integrated all-optical nonlinear activation function, experimentally realized through highly pump-depleted second-harmonic generation (SHG) in periodically poled lithium niobate (PPLN) nanophotonic waveguides, achieving 79% absolute conversion efficiency. This activation exhibits a sigmoid-like, wavelength-selective response with femtosecond-scale dynamics and light-speed processing, requiring no electrical control or auxiliary optical signals. We further validate its feasibility for neural inference by combining the measured SHG-based nonlinearity with linear operations implemented via a Mach–Zehnder interferometer system on a silicon PIC. Our demonstration achieves performance on par with digital implementations in real-world tasks, including airfoil regression and medical image classification. These results pave the way toward scalable, high-speed, and fully integrated all-optical neural networks for next-generation photonic AI hardware.

Introduction

Artificial general intelligence (AGI) has emerged as a widely pursued goal, showing the potential to revolutionize diverse fields such as climate prediction¹, autonomous driving², drug discovery³, controlled nuclear fusion⁴, and other areas of scientific research and engineering⁵. The accelerating progress toward AGI is driven by two key enablers: the continued advancement of high-performance computing hardware, which offer high-throughput computational power⁶; and the rapid evolution of large-scale AI models like large language models, which leverage this power to learn complex, high-dimensional representations from vast datasets⁷. However, the unprecedented scale and complexity of modern AI models are pushing the limits of conventional electronic computing architectures imposed by Moore’s law⁸. As model sizes reach hundreds of billions of parameters, the resulting computational demands present significant challenges in terms of bandwidth⁹, latency¹⁰, and energy efficiency¹¹. These limitations have sparked growing interest in alternative computing paradigms that can natively support the massive parallelism and data-intensive demands of increasing AI workloads. Optical computing—particularly in the form of optical neural networks (ONNs)—has emerged as a promising candidate, offering intrinsic advantages such as ultrafast signal transmission¹², passive data transport without resistive losses¹³, and capability for low-power, high-speed computation¹⁴.

Within the landscape of optical computing, photonic integrated circuits (PICs) stand out for their scalability and manufacturability¹⁵. By enabling dense integration of photonic components within low-loss waveguide structures, PICs support compact, CMOS-compatible architectures and provide a practical pathway toward large-scale, chip-level deployment of ONNs¹⁶. Mathematically, ONNs consist of two core components: linear operations, typically implemented as matrix multiplications, and nonlinear operations, which are essential for capturing complex pattern representations in latent feature spaces. Linear

operations are fundamental to feature embedding and signal transformation, and have been successfully demonstrated on PIC platforms using various photonic architectures. Examples include Mach–Zehnder interferometers (MZIs)^{17,18}, wavelength-division multiplexing (WDM)^{19,20}, optical metasurfaces^{21,22}, and phase-change materials^{23,24}. These advances highlight the growing maturity and strong potential of PIC-based systems for large-scale optical computing.

In contrast, realising optical nonlinear activation functions that can match the high performance of their linear counterparts remains a critical challenge for ONNs on PIC platforms¹³. Currently, most ONNs rely on incoherent optoelectronic approaches for nonlinear neuron activation, which involve optical-to-electrical conversion to detect optical power¹⁸. This process inevitably introduces latency and power inefficiencies and typically restricts activation functions to positive-only nonlinearities. To fully exploit the computational superiority of photonics, various all-optical nonlinear mechanisms have been explored, including laser bistability²⁵, semiconductor optical amplifiers (SOAs)²⁶, microring resonators (MRRs)^{27,28}, parametric processes^{29,30}, stimulated Brillouin scattering³¹ and material absorption^{32–35}. However, these methods generally require either electrical control signals or additional optical inputs to modulate or stimulate the nonlinear response. This adds operational overhead and routing complexity, increases response latency, and ultimately reduces the overall throughput of photonic computing systems. Therefore, a fully passive, all-optical nonlinear activation function—realized solely through integrated waveguide structures, operating without external signal or energy input, and capable of ultrafast response with light-speed processing—is highly desirable for scalable and high-throughput PIC-based ONN architectures.

In this work, we experimentally demonstrate, for the first time, a passive chip-based all-optical nonlinear activation function with a sigmoid-like response, completely free from external electrical or extra optical signals. The sigmoid function, a foundational nonlinearity in modern AI models⁷, is realized through a pump-depleted SHG process in a PPLN nanophotonic waveguide, achieving a high SHG conversion efficiency of approximately 79%, approaching state-of-the-art reported efficiencies³⁶. This enables the all-optical nonlinearity essential for learning decision boundaries in ONNs, with femtosecond-scale, wavelength-selective activation that supports computational frequencies exceeding 100 GHz, matching the performance of optical linear operations and enabling further gains through wavelength-division multiplexing. We then develop a silicon PIC specifically tailored for performing arbitrary matrix–vector multiplications using MZI networks. To demonstrate the feasibility of an optical neuron inference framework, nonlinear activation is implemented using the experimentally characterised input–output response of the PPLN waveguide, while linear operations are performed using a silicon photonic MZI-based PIC. We validate the performance of our principle across multiple machine learning tasks. The SHG-activated ONN demonstrates strong learning capability, accurately modeling complex decision boundaries in standard scikit-learn benchmarks. On a real-world airfoil self-noise regression task, it achieves accuracy comparable to traditional electronic implementations. In a more challenging medical image classification task, our ONN attains performance on par with state-of-the-art digital systems. This work marks an important step toward fully integrated, all-optical deep neural networks by bridging highly efficient nanophotonic optical parametric nonlinear processes with the rapidly evolving field of PIC-based optical computing.

Pump-depleted SHG-based all-optical nonlinear neuron activation

The core of our approach is the utilisation of the pump-depleted SHG in integrated PPLN waveguides as an all-optical nonlinear activation function. Under phase-matching condition, the fundamental harmonic (FH) wave undergoes energy transfer into the second harmonic (SH) wave, leading to efficient pump depletion and a saturating FH response. This interaction produces a sigmoid-like nonlinear transfer function, well-suited for neural network activation. The activation is implemented on a thin-film lithium niobate (TFLN) platform, which offers high second-order nonlinear susceptibility and supports efficient $\chi^{(2)}$ interactions^{37,38}. Efficient pump-depleted SHG is achieved in PPLN nanophotonic waveguides through periodic inversion of the crystal domains, enabling quasi-phase matching³⁹. By encoding computational information into the FH wave, the proposed nonlinear activation requires no external optical or electrical signals, making it fully passive, low-latency, and readily compatible with PICs. Fig. 1 illustrates the conceptual architecture of an optical neuron, where a PPLN waveguide array for nonlinear activation is applied after a MZI system that performs linear operations, together forming the basis for optical neural inference.

The system operates in three computational stages. (1) Following Clement’s optical computing architecture¹⁷, the input data vector $x = \{x_1, x_2, \dots, x_n\}$ is encoded into the FH at frequency ω , with the normalized data magnitude and sign represented by the amplitude A_n and phase ϕ_n of the transverse electric field component $E_n(\omega) = A_n e^{i(\omega t + \phi_n)}$. (2) The weight matrix is programmed via voltages applied to phase shifters within the MZI system. As the optical signals propagate through the network, matrix–vector multiplication is intrinsically performed through passive interference. (3) The output signals from the MZI system are utilized as the pump for the PPLN waveguides, where they undergo a pump-depleted SHG process. This induces a strong nonlinear transformation of the FH wave carrying the computational information, as described by equation (1), thereby realizing passive all-optical activation.

$$E(\omega, L) = E(\omega, 0) \frac{1}{\sqrt{\cosh^2(\Gamma L) + (\Delta k/2\Gamma)^2}} e^{-\alpha_\omega L} \quad (1)$$

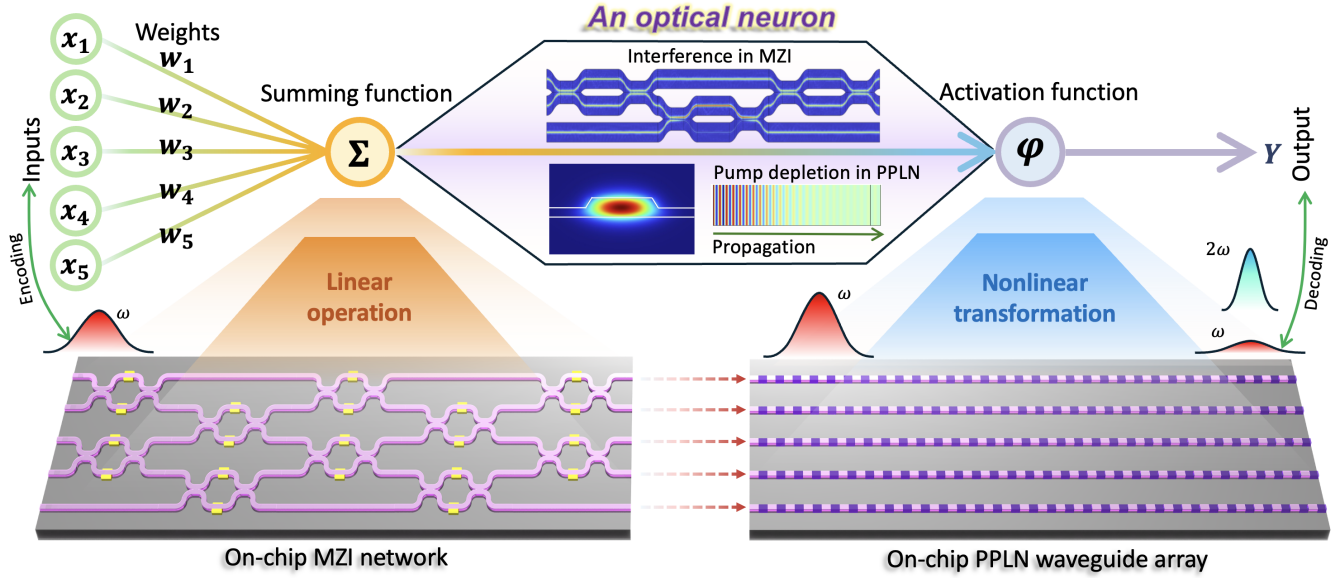


Figure 1. Conceptual diagram of an optical neuron employing pump-depleted SHG in PPLN waveguides for on-chip all-optical nonlinear activation following MZI-based linear operations. Neuron inputs are encoded in the amplitudes and phases of light at the fundamental harmonic frequency ω . The coherent optical signals carrying the inputs first pass through a MZI network, where linear operations are performed via optical interference. The outputs are then used as inputs to the PPLN nanophotonic waveguides, where nonlinear activation is achieved through efficient, passive pump-depleted SHG, enabled by quasi-phase matching and strong $\chi^{(2)}$ parametric interaction resulting from tight optical confinement in the TFLN platform. The neuron's output is extracted via homodyne detection at the same frequency. Although the current prototype employs two separate photonic chips, resulting in poor chip-to-chip integration and added electronic latency, this could be improved by fabricating everything on a single lithium niobate chip or via heterogeneous integration using photonic wire bonding.

where $E(\omega, 0)$ denotes the initial FH amplitude encoding the weighted sum of the neuron, and $E(\omega, L)$ represents the FH amplitude after the nonlinear interaction over a propagation length of L . The nonlinear coupling coefficient under quasi-phase matching conditions is given by $\Gamma = \frac{4\omega d_{\text{eff}} E(\omega, 0)}{\pi \sqrt{n_{\omega} n_{2\omega}} c}$, where c is the speed of light in vacuum, d_{eff} is the effective second-order nonlinear susceptibility, and n_{ω} and $n_{2\omega}$ are the effective indices of the FH and SH modes, respectively⁴⁰. In the ideal case of negligible phase mismatch ($\Delta k = 0$) and loss ($\alpha_{\omega} = 0$), the nonlinear activation function for the FH wave simplifies to $E(\omega, L) = E(\omega, 0) \text{sech}(\Gamma L)$, yielding a saturating sigmoid-like nonlinear transformation over a defined propagation length. This approach is inherently compatible with coherent photonic computing architectures that encode data in amplitude and phase. While the current prototype uses separate silicon and lithium niobate platforms for linear and nonlinear operations, respectively, future implementations through monolithic or heterogeneous integration could straightforwardly support fully optical, end-to-end photonic neural networks.

Results

Fabrications and characterizations of nonlinear and linear PICs

A 11-mm-long PPLN nanophotonic waveguide is fabricated to achieve the nonlinear transformation required for the activation function in the proposed optical neuron. The fabrication process is detailed in the Methods section. Fig. 2a(i) shows a scanning electron microscopy image of the waveguide cross-section, revealing the ridge geometry that ensures strong optical confinement for efficient nonlinear interaction. Fig. 2a(ii) presents a top-view confocal SHG image, confirming the periodic domain inversion and uniform quasi-phase matching along the waveguide. The experimental setup for characterizing the SHG response is illustrated in Fig. 2a(iii), where the generated SH and residual FH signals are separated by a wavelength-division multiplexer and detected by photodetectors. We measure the continuous-wave pumped SHG spectrum of the PPLN waveguide; Fig. 2b shows the normalized SHG intensity as a function of the pump power, indicating that the phase-matching wavelength is at 1552 nm, within the telecom C band. The output SH power and FH power are then measured as functions of the pump power in Fig. 2c. Experimental data points are fitted using a polynomial curve derived from fourth-order Runge–Kutta simulations of the coupled nonlinear wave equations governing pump-depleted SHG described by equation (1), demonstrating good agreement between the experimental results and the physical model. In the low-pump-power linear region, the device shows a normalized

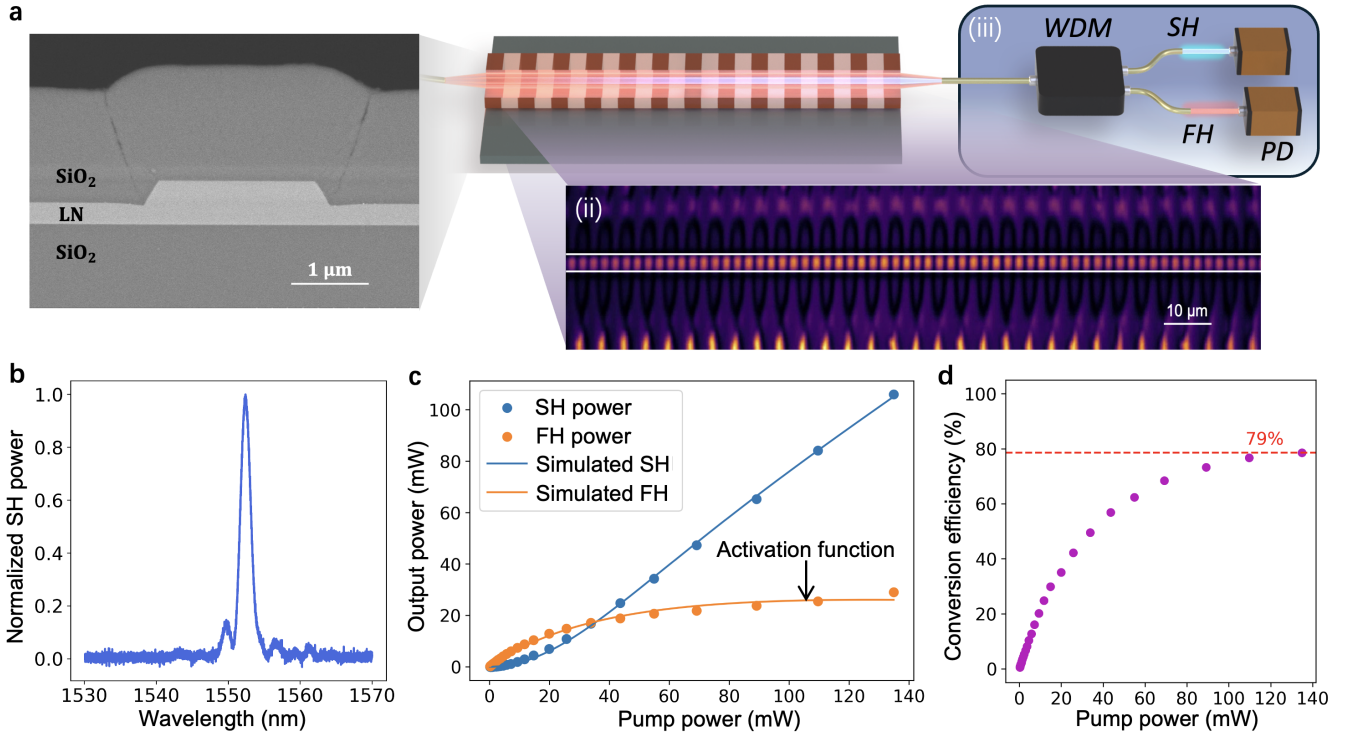


Figure 2. Pump-depleted SHG process in a PPLN nanophotonic waveguide measured for neuron nonlinear activation. **a** Fabrication and characterization of the nonlinear PPLN waveguide. (i) SEM image of the LN waveguide cross-section. (ii) Top-view laser-scanning SHG microscopic image of the PPLN waveguide. (iii) Measurement setup, where the output light from the PPLN waveguide is routed into a WDM, which separates the SH and FH light for detection with photodetectors (PD). **b** SHG spectrum of the PPLN waveguide, showing a phase-matching wavelength at 1552 nm. **c** Measured output power (dots) of the FH and SH light as a function of the pump power. The data is fitted by the fourth-order Runge–Kutta simulation results with scaling (curve), revealing a saturable, sigmoid-like nonlinearity for the FH light. **d** Calculated absolute conversion efficiency from the FH to SH as a function of pump power.

on-chip SHG conversion efficiency as high as $1986\% \pm 26\% \text{ W}^{-1}\text{cm}^{-2}$. The conversion efficiency starts to saturate at a pump power of ~ 10 mW, and reaches 79% (absolute) at 135 mW, as shown in Fig. 2d. As a result, the output power of the FH wave approximates a sigmoid-like nonlinearity within the measured power range, demonstrating the effectiveness of pump-depleted SHG in the PPLN waveguide as an all-optical nonlinear activation for the proposed optical neuron.

Figure 3a illustrates the MZI system used for linear operations, implemented on a PIC fabricated on a 220 nm silicon-on-insulator platform by Advanced Micro Foundry (Singapore). Thermo-optic phase shifters and on-chip germanium photodetectors are integrated to enable reconfigurable phase control and high-responsivity readout in the near-infrared. The input signal is evenly split into four channels using a series of 1×2 multimode interferometers, with two channels dedicated to subsequent computations and the other two reserved for detection and calibration. The design overall implements a two-dimensional arbitrary matrix–vector multiplier based on the Clements architecture¹⁷, and serves as the linear computing module in the proposed optical neuron. To characterize the MZI system’s performance, we conducted 300 measurements by supplying 60 sets of randomly generated 2×2 matrices (with elements normalized between 0 and 1), each repeated five times, and compared the measured outputs to the ground truth. As shown in Fig. 3b, the system achieved a rooted mean square error of 0.03, a standard deviation of 0.005, and a R^2 of 97.7%, demonstrating its high accuracy in performing analog matrix–vector multiplications. These results confirm the suitability of the developed MZI system as a robust weighted-sum module in the optical neuron architecture.

Demonstration of Nonlinear Expressiveness of SHG-based activation in PPLN

To evaluate the learning capability of our proposed method, we employ a fully connected neural network with a single hidden layer of 64 neurons, where the nonlinear activation function is based on the experimentally measured FH response from pump-depleted SHG in the PPLN waveguide (Fig. 2c), while the linear operations are implemented digitally. The activation function is modeled using a polynomial fit to the experimental data to enable gradient-based optimization during training.

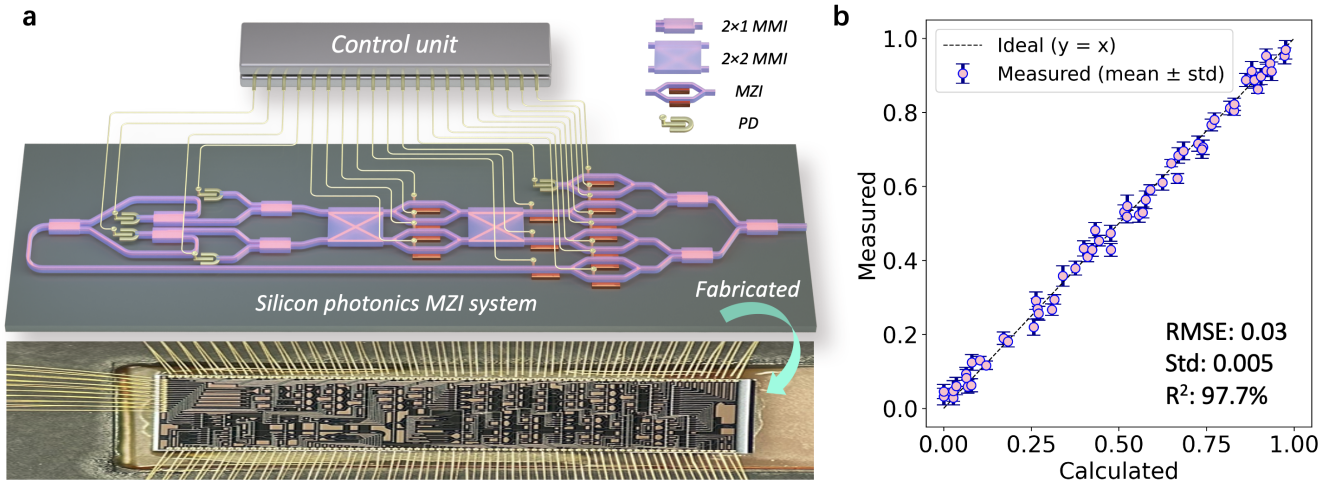


Figure 3. Design and characterization of the MZI system on a PIC for the linear operation required by the proposed optical neuron. **a** Schematic and microscopic image of the integrated silicon photonics-based MZI system, comprising on-chip multimode interferometers (MMIs), thermo-optic phase shifters, photodetectors (PDs), and wire bonding for electrical control. The system supports arbitrary 2×2 matrix–vector multiplication. **b** Experimental characterization of the PIC-based matrix multiplication using 100 random input vectors. The measured outputs demonstrate a root mean square error (RMSE) of 0.03, a standard deviation of 0.005, and an R^2 value of 97.7%, indicating sufficient fidelity for linear computation required by the optical neuron.

The training procedure is described in the Methods section. We first assess the model on three canonical binary classification benchmarks—Moon, Circle, and Gaussian datasets—from the Scikit-learn library⁴¹, each containing 120 samples evenly split for training and testing. Fig. 4a shows the raw data distributions with learned decision boundaries, where the nonlinear activation successfully adapts to varying geometric structures. As shown in Fig. 4b, the training losses decrease steadily with high test accuracies, suggesting good convergence and minimal overfitting. Receiver operating characteristic (ROC) curves in Fig. 4c show strong discriminative performance with area under the curves (AUCs) of 0.99 (Moon), 0.96 (Circle), and 0.97 (Gaussian). The final classification accuracies reach 0.92 (Moon), 0.90 (Circle), and 0.97 (Gaussian), respectively, demonstrating that the proposed SHG-based all-optical neuron activation mechanism can generate effective decision boundaries across diverse binary classification tasks.

We use the Iris dataset from Scikit-learn, as shown in Fig. 4d, to evaluate the SHG-based activation’s ability to generate decision surfaces in higher-dimensional feature space. As visualized in Fig. 4e, three features are activated to reduce visual complexity while preserving model fidelity. The resulting decision map shows well-separated regions for each class with distinct boundaries, demonstrating clear class confidence zones. The partial dependence in Fig. 4f reveal smooth and monotonic class transitions for each active feature. Probability shifts near decision thresholds reflect the proposed activation’s high sensitivity, enabling precise class separation with minimal variation in input features. Together, these results confirm the SHG-based nonlinear activation’s capability to construct expressive, localized decision boundaries, leading to a final classification accuracy of 99% on this multi-class task.

Regression on the Airfoil Self-Noise dataset with optical linear and nonlinear computing

To evaluate the computational compatibility of the SHG-based nonlinear activation with existing optical computing schemes, we further incorporate a silicon photonic MZI network to perform the matrix–vector multiplication required by the proposed optical neuron, as described in Fig. 1. Use of the MZI chip is described in the Methods section. We assess the combined performance of SHG-based activation and MZI-based linear transformation using a 64-neuron, fully connected, single-layer neural network on the NASA Airfoil Self-Noise regression dataset⁴². This dataset involves predicting sound pressure levels from five aerodynamic features as illustrated in Fig. 5a, presenting a more complex real-world challenge.

Figure 5b presents the training and evaluation process, showing the training loss alongside the evolving R^2 score on the test set. The SHG–MZI-based ONN exhibits stable convergence and ultimately achieves a final R^2 of 0.95, indicating strong predictive capability. By approaching the performance of its digital counterpart with same network architecture and electronic sigmoid activation, this result highlights the practical viability of our optical neuron architecture for complex regression tasks. Fig. 5c compares residuals with predicted values, and the accompanying histogram shows a narrow, symmetric distribution centered near zero, suggesting minimal systematic bias. The inset displays predicted versus true noise levels for both training

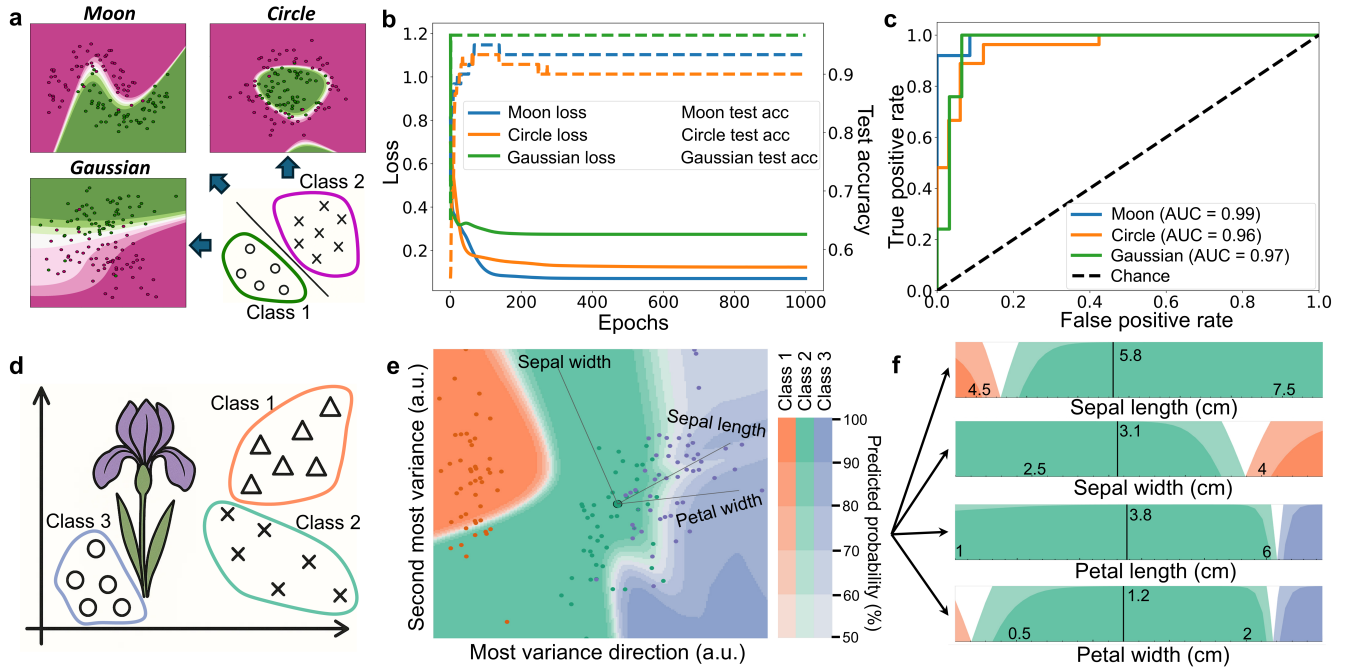


Figure 4. Evaluation of the nonlinear modeling ability of the proposed SHG-based all-optical neuron activation. **a** Decision boundaries generated by SHG-based neural networks for three binary classification datasets: Moon, Circle, and Gaussian. Pink and green dots represent two separable sets. **b** Training loss and testing accuracy curves over 1000 epochs, showing rapid convergence and stable performance across all binary datasets. **c** ROC curves and AUC scores demonstrate high classification performance: AUC = 0.99 (Moon), 0.96 (Circle), and 0.97 (Gaussian), significantly outperforming the chance level (dashed line). **d** Schematic diagram of Iris flower dataset consisting of three species. **e** 2-dimensional map of SHG-based model's decision surface around training data points, with axes representing directions in feature space based on principal component analysis. **f** Partial dependence shows predicted probability for a class changes along varied feature value. Black vertical line represents the current feature value of the selected instance.

and test sets, showing close alignment with the diagonal and further validating regression accuracy. Together, these results demonstrate that the SHG-activated optical neuron, combined with MZI-based linear operations, can effectively capture nonlinear relationships in real-world data.

Classification on dermatological images with optical linear and nonlinear computing

AI systems are increasingly effective in complex classification tasks. To further evaluate the capabilities of the proposed optical neuron that combines SHG-based activation with MZI-based linear operations, we test it on the DermaMNIST-C dataset⁴³, a 28×28-pixel dermatology subset of MedMNIST⁴⁴ comprising seven disease classes that cover 95% of clinically observed skin lesions. We implement a multilayer perceptron (MLP) as the baseline model, a foundational building block to model high-dimensional feature representations in modern AI systems. Each image is flattened into a 784-dimensional input vector and processed through an optical MLP with three hidden layers (256, 128, 64 neurons), as shown in Fig. 5d. The final hidden layer output is passed through a softmax layer to generate class probability distributions, as shown in Fig. 5e.

The training dynamics are illustrated in Fig. 5f, showing the evolution of loss and accuracy over epochs. During early training, the test accuracy briefly exceeds the training accuracy, indicating an effect commonly observed in small or imbalanced real-world datasets. As training progresses, the training accuracy steadily improves, while the test accuracy plateaus early once the model captures dominant generalizable features such as Nevi class. This behavior aligns with prior observations on DermaMNIST, where class imbalance and limited test-set variance can inflate early test accuracy⁴³. The final test accuracy reaches 82.66%, closely matching that of a digital ResNet-18 (82.50%), demonstrating that the MZI-SHG-based optical neural network generalizes well and effectively captures clinically relevant features in complex image classification tasks. The confusion matrix in Fig. 5g shows strong performance on Nevi (93.25%), the largest class, and reasonable accuracy on Lesion 2 (64.71%) and Carcinoma 2 (59.09%), indicating the model's ability to learn subtle diagnostic patterns. Overall, these results validate the effectiveness of the proposed SHG-based nonlinear activation, integrated with MZI-based linear operations, in enabling an ONN that achieves performance comparable to digital implementations on complex, high-dimensional medical

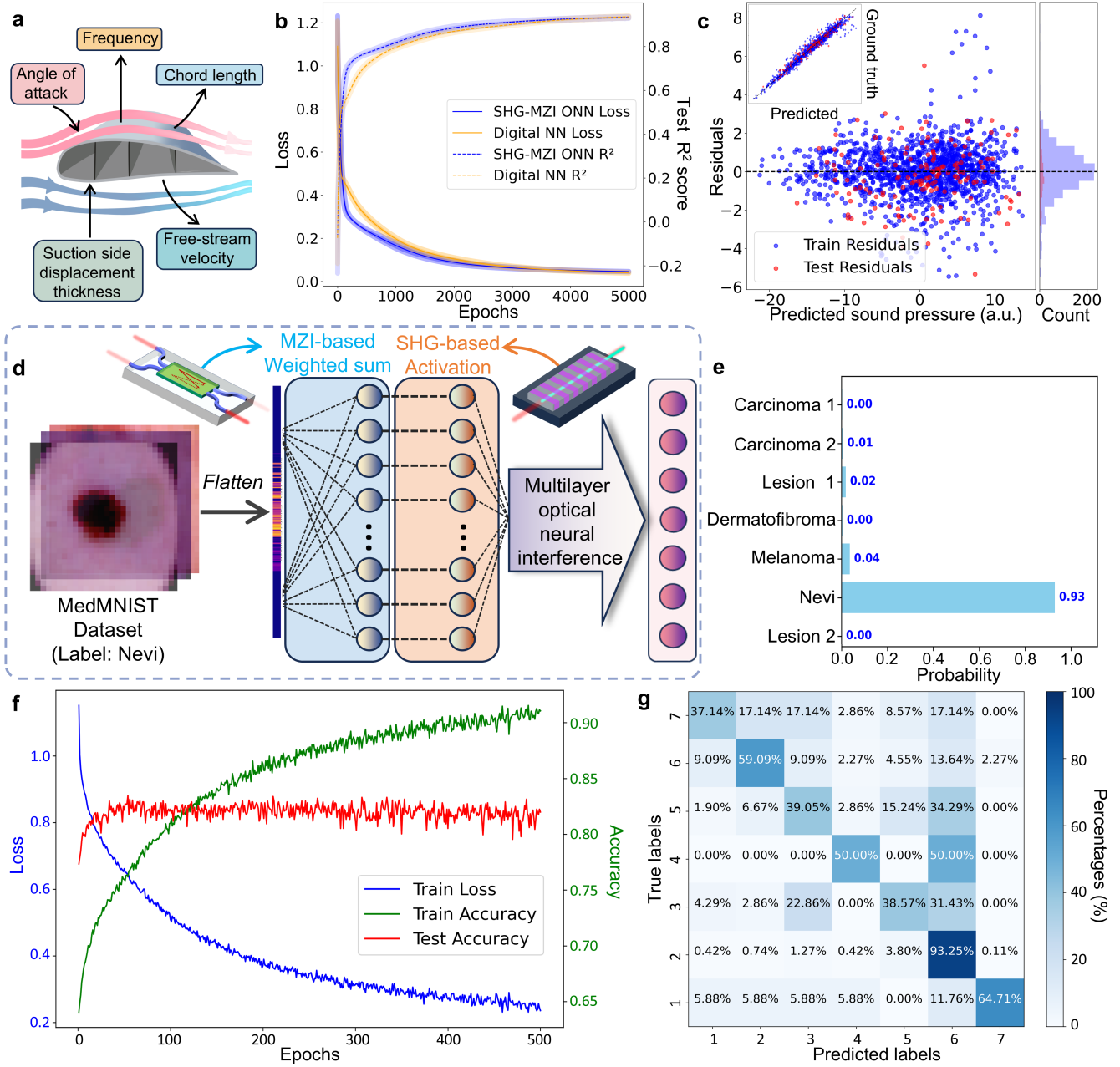


Figure 5. Evaluation of the SHG and MZI based ONNs on real-world regression and classification tasks. **a** A schematic representation of the Airfoil Self-Noise dataset with five aerodynamic features. **b** Training loss and test R^2 score over 5,000 epochs, demonstrating the ONN's stable convergence. **c** Residuals plotted against predicted values, with an accompanying histogram showing their distribution centered around zero. The inset displays predicted versus true sound pressure levels, demonstrating strong agreement along the ideal diagonal, indicating accurate model fitting. **d** Inference pipeline of the proposed optical neurons on the MedMNIST dataset. The input image is first flattened into a vector and encoded into the amplitudes and phases of optical signals. These signals undergo a linear weighted-sum operation via MZI-based interference, producing hidden-layer representations. The outputs are then nonlinearly activated using the fitted FH response curve derived from experimentally measured pump-depleted SHG data. After passing through multiple layers of MZI-SHG-based transformations, the final output is fed into a softmax layer to generate the prediction distribution. **e** Example prediction probability distribution for a nevi class generated by the ONN. **f** Training loss, accuracies, and test accuracy over epochs on the DermaMNIST-C dataset. **g** The confusion matrix of the MLP model trained on the dataset.

image classification tasks.

Table 1. Comparison of state-of-the-art sigmoid-shaped optical nonlinear activation functions.

	Passivity	Response time	Computational frequency	Time-of-flight	Wavelength selectivity	Integration scalability
SOA ²⁶	No	~100 ps	~10 GHz	~10 ps	No	Low
MZI & MRR ²⁷	No	>38 ps	<26 GHz	~10 ps	No	High
Ge-Si photodiode ³²	No	51 ps	~20 GHz	0.11 ps	No	Moderate
P-N modulator ²⁸	No	~100 ps	~5 GHz	105 ps	No	High
Brillouin amplifier ³¹	No	>10 ns	~100 MHz	500 ns	Yes	Low
This work	Yes	~ 1 fs ⁴⁰	>100 GHz	81 ps	Yes	High

Discussion

We present a passive all-optical nonlinear activation method based on experimentally demonstrated pump-depleted SHG in a PPLN nanophotonic waveguide, featuring a high absolute conversion efficiency of 79%. This parametric process induces an ultrafast, sigmoid-like nonlinear response through depletion of the FH light carrying computational information, without requiring additional signals or energy input. Leveraging the maturity of silicon photonics, we demonstrate an optical neuron inference architecture that combines a silicon photonic MZI system for optical matrix computation with experimentally grounded SHG-based nonlinear activation. Experimental results show that this approach achieves accuracy comparable to state-of-the-art electronic implementations on real-world machine learning tasks, including airfoil noise regression and medical image classification, validating the effectiveness and feasibility of the architecture.

From a machine learning perspective, the sigmoid function remains a foundational activation due to its boundedness, differentiability, and biological plausibility⁴⁵. However, efficient all-optical realizations of sigmoid-shaped responses within PIC-based ONNs are scarce. In electronic systems, computing a single sigmoid-shaped function typically incurs a delay on the order of tens of nanoseconds⁴⁶, generally contributing minimally to the overall inference time dominated by dense linear operations. In contrast, ONNs can perform all-optical linear transformations at computational frequencies exceeding 100 GHz, offering up to 100-fold faster processing than conventional electronics⁴⁷. To fully harness the computational potential of photonics, it is essential to realize nonlinear operations that match this speed and exhibit an ultrafast response, thereby enabling full exploitation of the vast bandwidth inherent to light. To facilitate a comprehensive comparison, we summarize existing all-optical nonlinear activation mechanisms with sigmoid-like characteristics in Table 1, focusing on five key metrics. Passivity is critical for energy efficiency, reduced control complexity, and architectural simplicity. Response time reflects the material's intrinsic speed in reacting to light, governing how quickly individual operations can be executed. Computational frequency represents the upper bound of sustained processing capacity, determining the system's maximum achievable throughput. Integration scalability indicates the potential for implementing deep ONNs on a unified photonic chip.

Most previously reported methods rely on active modulation schemes, with response speeds fundamentally constrained by carrier dynamics or electronic control circuitry. As a result, they typically exhibit response times on the order of tens of picoseconds, limiting their computational frequencies below tens of GHz. In contrast, our approach leverages a fully passive parametric mechanism with a built-in near-instantaneous optical response in the femtosecond regime^{40,48}, thereby inherently supporting computational frequencies exceeding 100 GHz. This performance aligns with that of state-of-the-art all-optical linear processing rates and removes a fundamental bottleneck in constructing fully photonic neural systems. Although the current 11 mm PPLN waveguide introduces a relatively long time-of-flight delay, this does not pose a computational limitation as optical computing derives its benefits primarily from high throughput rather than propagation speed⁴⁹. Moreover, our proposed activation is implemented using a compact straight waveguide geometry without requiring additional epitaxy, facilitating fabrication simplicity, minimal optical footprint, and excellent cascability, all of which are critical for future multilayer ONN scalability. The intrinsic wavelength selectivity of the SHG process also enables compatibility with wavelength-division multiplexing, offering the potential to further increase data throughput³¹. Taken together, these features position our approach as a promising pathway toward practical, high-speed, and scalable integrated all-optical neural networks.

The current optical neuron prototype combines a silicon MZI network for linear operations with a pump-depleted SHG response measured in PPLN waveguides on a TFLN platform for nonlinear activation, successfully demonstrating the feasibility of performing neural inference using separate all-optical processes. Nevertheless, operating across two discrete chips imposes limitations similar to those encountered in electronic systems, including power inefficiencies, timing overhead, optical power

mismatches, and additional coupling and insertion losses. Future efforts may explore heterogeneous integration strategies that consolidate both linear and nonlinear functionalities onto a hybrid silicon–lithium niobate platform⁵⁰, reducing optical losses and improving power compatibility. Alternatively, migrating both operations onto a monolithic TFLN platform offers a promising route toward fully integrated ONN architectures, benefiting from higher modulation speeds enabled by LN’s large electro-optic coefficient and reduced fabrication complexity³⁷. Moreover, adopting pulse-pump schemes for data encoding and computation can further reduce overall energy consumption by leveraging short, high-peak-power optical pulses, thereby enhancing the efficiency of all-optical nonlinear activation. In the future, PPLN microring resonators may also help to reduce the required pump power, as well as the overall footprint, due to the strong field enhancement available within the resonator. Realizing a fully integrated, all-optical neural network on a single chip remains a key milestone for next-generation photonic neuromorphic computing.

Methods

PPLN nanophotonic waveguide fabrication

We fabricate the PPLN nanophotonic waveguides on a 600 nm thick MgO-doped x-cut TFLN chip. Comb-like electrodes with a pitch of 4.75 μm and duty cycle of 50% are patterned using a combination of electron-beam (e-beam) lithography, followed by e-beam metal evaporation and lift-off. We apply a series of electrical pulses to periodically reverse the polarity for PPLN waveguides. A top-view laser-scanning SHG imaging of the PPLN waveguide is shown in Fig. 1a(ii). After poling, the waveguides are patterned using e-beam lithography and Ar^+ etching by inductively coupled plasma reactive ion etching (ICP-RIE), with hydrogen silsesquioxane (HSQ) e-beam resist as the etching mask. Finally, the chip is covered with 1.65 μm silicon oxide by plasma-enhanced chemical vapor deposition (PECVD). A cross-section SEM image is shown in Fig. 1a(i).

Training procedure

All models are trained using Python 3.9 with the PyTorch framework⁵¹, and training is accelerated using a CUDA-enabled graphics processing unit (NVIDIA RTX 4090, 24GB RAM). Each model is trained with task-specified epochs using the Adam optimizer with an initial learning rate of 10^{-3} and L_2 regularization to mitigate overfitting. Cross-entropy loss is employed as the objective function, with a batch size of 128. A learning rate scheduler reduces the learning rate by a factor of 10 after 40% and 80% of the total training epochs to facilitate convergence. To enhance generalization in the medical image classification task, dropout is applied to the hidden layers with a rate of 0.2. Additionally, batch normalisation is employed after each linear transformation to stabilise training and improve gradient flow.

Implementation details

The obtained weight matrix after training for each optical neuron is partitioned into 2×2 submatrices and mapped onto the fabricated silicon photonics-based universal linear processor. The i -th submatrix A_i is decomposed via singular value decomposition as $A_i = U_i \Sigma_i V_i$, where U_i and V_i are unitary matrices and Σ_i is a diagonal matrix. Following the Clements design, diagonal matrices are implemented using arrays of amplitude phase shifters with transfer matrices of the form $D = \text{diag}(e^{i\phi_1}, e^{i\phi_2})$, while unitary matrices are realized using MZIs, whose transfer matrix is given by the following:

$$T = ie^{\frac{i\theta}{2}} \begin{bmatrix} e^{i\phi_3} \sin\left(\frac{\theta}{2}\right) & e^{i\phi_3} \cos\left(\frac{\theta}{2}\right) \\ \cos\left(\frac{\theta}{2}\right) & -\sin\left(\frac{\theta}{2}\right) \end{bmatrix} \quad (2)$$

The reprogrammability of the processor is facilitated by precise tuning of both internal and external MZI phase shifts, denoted by θ and ϕ_i . These phase shifts are adjusted using resistive heaters based on strong thermo-optic effect in silicon.

$$\Delta\Phi = \left(\frac{2\pi L}{\lambda_0}\right) \left(\frac{dn}{dT}\right) \epsilon V^2 \quad (3)$$

Here, $L = 100 \mu\text{m}$ denotes the length of the heater, $\lambda_0 = 1550 \text{ nm}$ is the vacuum wavelength of the on-chip coupled light, and the thermo-optic coefficient of silicon at 300 K is $\frac{dn}{dT} = 1.86 \times 10^{-4} \text{ K}^{-1}$. The constant ϵ accounts for thermal properties including heat capacity and resistance. The phase shift induced by a single heater exhibits a square-law dependence on the applied voltage. In the proposed optical neuron, both inputs and weight matrices are encoded through voltage-controlled phase shifts. When optical signals are injected, the silicon photonic MZI system performs the corresponding linear operations in the optical domain.

References

1. Bi, K. *et al.* Accurate medium-range global weather forecasting with 3d neural networks. *Nature* **619**, 533–538 (2023).
2. Ma, Y., Wang, Z., Yang, H. & Yang, L. Artificial intelligence applications in the development of autonomous vehicles: A survey. *IEEE/CAA J. Autom. Sinica* **7**, 315–329 (2020).
3. Jiménez-Luna, J., Grisoni, F. & Schneider, G. Drug discovery with explainable artificial intelligence. *Nat. Mach. Intell.* **2**, 573–584 (2020).
4. Degraeve, J. *et al.* Magnetic control of tokamak plasmas through deep reinforcement learning. *Nature* **602**, 414–419 (2022).
5. Wang, H. *et al.* Scientific discovery in the age of artificial intelligence. *Nature* **620**, 47–60 (2023).
6. Garisto, D. How cutting-edge computer chips are speeding up the ai revolution. *Nature* **630**, 544–546 (2024).
7. LeCun, Y., Bengio, Y. & Hinton, G. Deep learning. *Nature* **521**, 436–444 (2015).
8. Williams, R. S. What's next?[the end of moore's law]. *Comput. Sci. & Eng.* **19**, 7–13 (2017).
9. Reuther, A. *et al.* Survey of machine learning accelerators. In *2020 IEEE high performance extreme computing conference (HPEC)*, 1–12 (IEEE, 2020).
10. Huang, Y. *et al.* Memristor-based hardware accelerators for artificial intelligence. *Nat. Rev. Electr. Eng.* **1**, 286–299 (2024).
11. Bourzac, K. Fixing ai's energy crisis. *Nature* (2024).
12. Shastri, B. J. *et al.* Photonics for artificial intelligence and neuromorphic computing. *Nat. Photonics* **15**, 102–114 (2021).
13. Farmakidis, N., Dong, B. & Bhaskaran, H. Integrated photonic neuromorphic computing: opportunities and challenges. *Nat. Rev. Electr. Eng.* **1**, 358–373 (2024).
14. Oguz, I. *et al.* Resource-efficient photonic networks for next-generation ai computing. *Light. Sci. & Appl.* **14**, 34 (2025).
15. Hua, S., Divita, E., Yu, S. *et al.* An integrated large-scale photonic accelerator with ultralow latency. *Nature* **640**, 361–367 (2025).
16. Zhou, H. *et al.* Photonic matrix multiplication lights up photonic accelerator and beyond. *Light. Sci. & Appl.* **11**, 30 (2022).
17. Clements, W. R., Humphreys, P. C., Metcalf, B. J., Kolthammer, W. S. & Walmsley, I. A. Optimal design for universal multipoint interferometers. *Optica* **3**, 1460–1465 (2016).
18. Xu, Z. *et al.* Large-scale photonic chiplet taichi empowers 160-tops/w artificial general intelligence. *Science* **384**, 202–209 (2024).
19. Feldmann, J., Youngblood, N., Wright, C. D., Bhaskaran, H. & Pernice, W. H. All-optical spiking neurosynaptic networks with self-learning capabilities. *Nature* **569**, 208–214 (2019).
20. Ohno, S., Tang, R., Toprasertpong, K., Takagi, S. & Takenaka, M. Si microring resonator crossbar array for on-chip inference and training of the optical neural network. *Acs Photonics* **9**, 2614–2622 (2022).
21. Fu, T. *et al.* Photonic machine learning with on-chip diffractive optics. *Nat. Commun.* **14**, 70 (2023).
22. Wang, Z., Chang, L., Wang, F., Li, T. & Gu, T. Integrated photonic metasystem for image classifications at telecommunication wavelength. *Nat. communications* **13**, 2131 (2022).
23. Feldmann, J. *et al.* Parallel convolutional processing using an integrated photonic tensor core. *Nature* **589**, 52–58 (2021).
24. Dong, B. *et al.* Higher-dimensional processing using a photonic tensor core with continuous-time data. *Nat. Photonics* **17**, 1080–1088 (2023).
25. Crnjanski, J., Krstić, M., Totović, A., Pleros, N. & Gvozdić, D. Adaptive sigmoid-like and prelu activation functions for all-optical perceptron. *Opt. Lett.* **46**, 2003–2006 (2021).
26. Mourgas-Alexandris, G. *et al.* An all-optical neuron with sigmoid activation function. *Opt. express* **27**, 9620–9630 (2019).
27. Jha, A., Huang, C. & Prucnal, P. R. Reconfigurable all-optical nonlinear activation functions for neuromorphic photonics. *Opt. letters* **45**, 4819–4822 (2020).
28. Bandyopadhyay, S. *et al.* Single-chip photonic deep neural network with forward-only training. *Nat. Photonics* **18**, 1335–1343 (2024).
29. Li, G. H. *et al.* All-optical ultrafast relu function for energy-efficient nanophotonic deep learning. *Nanophotonics* **12**, 847–855 (2023).

30. Basani, J. R., Heuck, M., Englund, D. R. & Krastanov, S. All-photonics artificial-neural-network processor via nonlinear optics. *Phys. Rev. Appl.* **22**, 014009 (2024).
31. Slinkov, G., Becker, S., Englund, D. & Stiller, B. All-optical nonlinear activation function based on stimulated brillouin scattering. *Nanophotonics* (2025).
32. Shi, Y. *et al.* Nonlinear germanium-silicon photodiode for activation and monitoring in photonic neuromorphic networks. *Nat. Commun.* **13**, 6048 (2022).
33. Chen, C. *et al.* Ultra-broadband all-optical nonlinear activation function enabled by mote2/optical waveguide integrated devices. *Nat. Commun.* **15**, 9047 (2024).
34. Xu, Z. *et al.* Reconfigurable nonlinear photonic activation function for photonic neural network based on non-volatile opto-resistive ram switch. *Light. Sci. & Appl.* **11**, 288 (2022).
35. Zhong, C. *et al.* Graphene/silicon heterojunction for reconfigurable phase-relevant activation function in coherent optical neural networks. *Nat. Commun.* **14**, 6939 (2023).
36. Chen, P.-K. *et al.* Adapted poling to break the nonlinear efficiency limit in nanophotonic lithium niobate waveguides. *Nat. Nanotechnol.* **19**, 44–50 (2024).
37. Zhu, D. *et al.* Integrated photonics on thin-film lithium niobate. *Adv. Opt. Photonics* **13**, 242–352 (2021).
38. Shi, X. *et al.* Efficient photon-pair generation in layer-poled lithium niobate nanophotonic waveguides. *Light. Sci. & Appl.* **13**, 282 (2024).
39. Wang, C. *et al.* Ultrahigh-efficiency wavelength conversion in nanophotonic periodically poled lithium niobate waveguides. *Optica* **5**, 1438–1441 (2018).
40. Boyd, R. W., Gaeta, A. L. & Giese, E. Nonlinear optics. In *Springer Handbook of Atomic, Molecular, and Optical Physics*, 1097–1110 (Springer, 2008).
41. Pedregosa, F. *et al.* Scikit-learn: Machine learning in python. *J. machine Learn. research* **12**, 2825–2830 (2011).
42. Brooks, T., Pope, D. & Marcolini, M. Airfoil self-noise. *UCI Mach. Learn. Repos.* **10**, C5VW2C (2014).
43. Abhishek, K., Jain, A. & Hamarneh, G. Investigating the quality of dermamnist and fitzpatrick17k dermatological image datasets. *Sci. Data* **12**, 196 (2025).
44. Yang, J. *et al.* Medmnist v2-a large-scale lightweight benchmark for 2d and 3d biomedical image classification. *Sci. Data* **10**, 41 (2023).
45. Szandała, T. Review and comparison of commonly used activation functions for deep neural networks. *Bio-inspired neurocomputing* 203–224 (2021).
46. Shakiba, F. M. & Zhou, M. Novel analog implementation of a hyperbolic tangent neuron in artificial neural networks. *IEEE Transactions on Ind. Electron.* **68**, 10856–10867 (2020).
47. Shen, Y. *et al.* Deep learning with coherent nanophotonic circuits. *Nat. photonics* **11**, 441–446 (2017).
48. Schumacher, Z. *et al.* Nanoscale force sensing of an ultrafast nonlinear optical response. *Proc. Natl. Acad. Sci.* **117**, 19773–19779 (2020).
49. McMahon, P. L. The physics of optical computing. *Nat. Rev. Phys.* **5**, 717–734 (2023).
50. He, M. *et al.* High-performance hybrid silicon and lithium niobate mach–zehnder modulators for 100 gbit s⁻¹ and beyond. *Nat. photonics* **13**, 359–364 (2019).
51. Paszke, A. *et al.* Pytorch: An imperative style, high-performance deep learning library. *Adv. neural information processing systems* **32** (2019).

Acknowledgements

We acknowledge seed funding from the National University of Singapore through the NUS Artificial Intelligence Institute, National Research Foundation (NRF-NRFF15-2023-0005), as well as funding from A*STAR (M23M7c0125).

Author contributions

W.F. and X.S. contributed equally to this work. W.F., X.S., and A.D. conceived the idea and co-wrote the manuscript. W.F., X.S., S.S.M., and Y.G. designed the experiments and carried out device fabrication. W.F. and L.S. developed the simulations. W.F. and Z.W. conducted the literature review. A.D. and D.Z. supervised the project. All authors contributed to the discussion of results and reviewed the manuscript.

Competing interests

The authors declare no competing interests.